Article

Scattering Fourier Transform Biosensor (SFTB): Binary Mixture Consisting of Magnetic Ni Nanorings and Plasmonic Au Nanorods

Hajir Hilal, Sungwoo Lee, Insub Jung, Sungjae Yoo, and Sungho Park

Anal. Chem., **Just Accepted Manuscript** • DOI: 10.1021/acs.analchem.0c02065 • Publication Date (Web): 26 Jun 2020

Scattering Fourier Transform Biosensor (SFTB): Binary Mixture Consisting of Magnetic Ni Nanorings and Plasmonic Au Nanorods

Hajir Hilal[a†], Sungwoo Lee[a†], Insub Jung[a,b], Sungjae Yoo [a], and Sungho Park[a]*

[a]Department of Chemistry, Sungkyunkwan University, Suwon, 16419, South Korea

[b]Current affiliation: Department of Chemistry, Northwestern University, Evanston, IL

*Email: spark72@skku.edu

ABSTRACT

We report a biosensing platform based on a binary mixture comprised of Au nanorods (plasmonic nanoparticles, Au NRs) and magnetically responsive Pt@Ni nanorings (magnetic nanostirrers, MN-rings). The mixture of Au NRs and MN-rings was modulated with an external rotating magnetic field (a dynamic assay with magnetic perturbation), which led to fluctuating extinction on UV-Vis spectroscopy measurement. As the surfaces of Au NRs were modified with antigens and antibodies, their periodic profile of extinction changed in accordance with surface modification of Au NRs. The obtained periodic extinction with time could be converted to a frequency domain function where the signal-to-noise ratios of the peaks were evaluated to monitor surface bio-recognitions on Au NRs, which is in contrast to conventional biosensors (a stagnant assay without perturbation) that use only the peak shift of localized surface plasmon resonance of Au nanoparticles

Introduction

Localized surface plasmon resonance (LSPR) is collective oscillation of conduction electrons at the surface of metal nanoparticles (i.e., Au, Ag, Cu, or Al), which is driven by irradiated electromagnetic waves.[1-2] It is well known that LSPR changes as a function of size and shape of nanostructures and varies in response to changes in refractive index of the medium surrounding plasmonic materials. Given that the highly confined oscillating electric fields extend into the surroundings, and their resonance conditions are very dependent on refractive index, many LSPR sensors have been developed for detection of DNA and protein-protein interactions and antigen-antibody recognition.[3-5] The detection principles of this label-free and highly sensitive LSPR sensors are based on the shift of LSPR peak wavelength upon adsorption of biomolecules on nanoparticles.[6-9] However, in many cases, peak shifts accompany the damping of LSPR bands, which hinders further lowering the detection of limit.[10-11] To improve the merits of LSPR sensors, several strategies have been adopted: utilization of gold nanoparticles with diverse morphology (e.g., nanorods,[12-13] nanobipyramids,[14] and nanostars[15]), combination of a signal enhancer whose molecular resonance can be coupled with an LSPR spectral band to amplify LSPR band shift,[16] increase in mass of the target molecules to enhance the change in local refractive index,[17-18] and incorporation of magnetically responsive components to endow magnetic modulation.[19-22] In particular, magnetically modulable plasmonic nanoparticles have exhibited instant and selective excitation of plasmon modes depending on field direction (i.e., orientation of nanoparticles) with respect to the direction of incidence and polarization of light, which is both unique and not feasible with non-magnetic plasmonic nanoparticles.[21-27] However, to modulate plasmonic nanomaterials with an external magnetic field, magnetically responsive components need to be linked to the plasmonic

nanomaterial, majorly limiting to core-shell nanoparticles or multi-segmented hybrid nanocomposites.[28-30]

Herein, we demonstrate how a binary mixture biosensor platform can be established by mixing Au nanorods (Au NRs) and magnetically responsive Pt@Ni nanorings (MN-rings). Scheme 1 describes the experimental set-up and the operating concept for monitoring bio-recognition reactions. A tunable external rotating magnetic field was applied to the cuvette containing Au NRs and MN-rings, where bio-recognition exclusively occurs on the surface of Au, and the whole solution is agitated locally but homogeneously by dispersed MN-rings, leading to fluctuating extinction and accordingly the sensing signals. Au NRs exhibit a unique LSPR band at a specific wavelength (i.e., depending on size and shape), and the band red-shifts as the surface is consecutively modified with antibody and antigen, mainly due to the change of refractive index. In contrast, MN-rings do not exhibit noticeable LSPR features but have a broad extinction over the entire range of wavelengths. When an external rotating magnetic field is applied, MN-rings generate a periodically fluctuating optical response (depicted by gray traces in Scheme 1B), and the presence of surface-modified Au NRs exhibits a characteristic LSPR at the observed wavelength. Under magnetic rotation and at the observed wavelength, the sum of extinctions was monitored as a function of time, and the typical periodic sigmoidal function was generated, as shown in Scheme 1C. As antigens bind the antibodies anchored to the surfaces of Au NRs, the LSPR band is systematically red-shifted.

Under the same magnetic rotation and at the same observed wavelength, the sigmoidal function changes its fluctuating profile because the sum of LSPR band intensities (from black to light blue profile) and scattering intensity of MN-rings (gray traces) decreases from 1 to 3. MN-rings exhibit broad featureless extinction over the entire spectral range, but Au NRs

generate the characteristic LSPR band within the investigated spectral range. It is noteworthy that the presence of magnetically inert Au NRs behaves as noise to extinction (mainly scattering) fluctuation of MN-rings, and the resulting sigmoidal functions become more distinct as the peak intensity of Au NRs deviates from the observed wavelength. The noise decrease results in an amplitude increase of extinction periodic fluctuation with magnetic rotations (Scheme 1C). When the periodically fluctuating optical responses are converted to a frequency domain function through FFT, the peak intensity increases as a function of concentration of antigen (Scheme 1D). This detection strategy enables distinctive detection of antigens with higher sensitivity, lower detection limit, and tailorable dynamic range, in sharp contrast to conventional assays based only on LSPR shifts.

Experimental section

Instrumentation

An FEL Tecnai-F30 was used to acquire transmission electron microscopy (TEM) images. Scanning electron microscopy (SEM) images were obtained using JEOL JSM-7100F and JSM-7800F instruments. UV-vis-NIR absorption spectra were obtained using a S-3100 (Scinco) spectrophotometer and a UV-3600 (Shimadzu) spectrophotometer. Zeta potential of nanoparticles was obtained using the DLS instrument (Zetasizer NanoZs90, Malvern).

Synthesis of magnetic nanostirrers MN-rings

Au nanodisks[31] were synthesized by manipulation of Au triangular nanoplates, and Au nanoprisms[32] were prepared from 5 nm spherical seeds by a three-step, seed-mediated method

with iodide ions, as reported previously. For this, 1.5 ml of a mixture of 10 ml of 0.05 M CTAB and 250 μL of 20 mM $HAuCl_4 \cdot 3H_2O$ was added to 10 ml of Au nanoprism solution. After 1 hr, the reaction was completed. The synthetic pathway for rim-preferential growth of Pt on Au nanoplates followed the experimental procedure in our previous paper.[33] In the presence of iodide ion (50 μM), 20 mL of 0.05 M CTAB, 5 mL of redispersed Au nanoplates, 30 μL of 2 mM aqueous $AgNO_3$ solution, and 480 μL of 0.1 M aqueous ascorbic acid solution were added to a vial. The mixture was kept at 70 °C. After 1 h, 480 μL of 0.1 M HCl and 300 μL of 2 mM aqueous H_2PtCl_6 solution were added to the mixture with gentle shaking. The mixture was kept at 70 °C for approximately 4 h. After this reaction, the sample was centrifuged, and the supernatant was removed and re-dispersed in DI water. After washing twice, Au@Pt nanoplates were dispersed in 15 mL of DI water for preparation of stock solution. To prepare Pt ring NPs by etching the central Au section of Au@Pt nanoplates, 2 mL of 0.05 M CTAB with iodide ions (50 μM), 100 μL of 2 mM aqueous $HAuCl_4$ solution, and 1 mL of Au@Pt nanoplate stock solution were added to the vial. The mixture was kept at 50 °C for 30 min. Next, for deposition of nickel, 1 mL of Pt ring-NPs dispersed in 0.05 M CTAB was added to a mixture containing 8.7 mL of triply deionized water, 20 μL of 0.25 M $NiCl_2$, and 120 μL of N_2H_4 (hydrazine solution). The solution was kept in a 50 ℃ oven for 2 hrs. Then the product was washed two times with triply deionized water followed by centrifugation at 4000 rpm for 15 min; after each washing step, magnetic NPs were collected using a permanent magnet.

Synthesis of magnetic nanostirrers Ni MNSs

MNSs were synthesized by a three-step, seed mediated method: (1) Synthesis of Au nanospheres (Au NSs), (2) Deposition of Pt onto Au nanospheres (synthesis of Au@Pt nanospheres (Au@Pt NSs)), and (3) Deposition of Ni onto Au@Pt NSs (synthesis of MNSs).

Synthesis of Au NSs

To synthesize seed solution for Au NSs, 5 ml of 20 mM $HAuCl_4$ solution was added to 195 ml of triply deionized water (Millipore), which was then boiled.[34] To this solution, 10 ml of 38.8 mM trisodium citrate dihydrate was added, and the mixture was boiled for 20 min. To prepare Au NSs, 4 ml of 20 mM $HAuCl_4$ solution and 0.4 ml of 10 mM $AgNO_3$ were added to 167 ml of triply deionized water, which was then mixed with 3 ml of the aforementioned 13 nm Au NS solution. Next, 30 ml of 5 mM ascorbic acid was slowly added (0.500 ml/min) while vigorously stirring the solution. The resulting diameter of as-synthesized Au NSs was determined to be 53 ± 3 nm.

Synthesis of Au@Pt NSs

To prepare Au@Pt NSs, 10 ml of as-synthesized Au NSs were added to the growth solution of 25 ml of 0.1 M CTAB, 940 μl of 0.1 M ascorbic acid, 940 μl of 0.1 M hydrochloric acid, and 600 μl of 2 mM H_2PtCl_6 solution in the presence of iodide ion (50 μM). The solution was heated to 50 ℃ in an oven and kept for 9 h. Thereafter, the solution was washed twice with triply deionized water by centrifugation.

Synthesis of MNSs

Deposition of nickel onto the Au@Pt NSs was conducted using the modified protocol reported by the Liz Marzan group.[35] To prepare MNSs, 7.7 ml of triply deionized water, 1 ml of 0.1 M

CTAB, 160 μl of 0.25 M nickel chloride solution, 480 μl of 2.5 M hydrazine solution, and 1 ml of optically normalized as-synthesized Au@Pt NSs were added to a vial. The solution was heated in an oven to 50 ℃ and kept for 3 h, followed by washing twice with triply deionized water. Each washing step was carried out with a permanent magnet to effectively collect MNSs.

Synthesis of gold nanorods (Au NRs)

Au NRs were synthesized using the seed-mediated method. To prepare the seed solution for Au NRs, 0.6 ml of ice-cold 10 mM $NaBH_4$ was added to a solution containing 10 ml of 0.1 M CTAB and 125 μl of 20 mM $HAuCl_4$ under vigorous stirring. The seed solution was aged for 10 min at room temperature before use. Then, 23.75 ml of 0.1 M CTAB, 0.625 ml of 20 mM $HAuCl_4$, 137.5 μl of 0.1 M ascorbic acid, 10 mM of 150 μl of $AgNO_3$, and 30 μl of as-prepared seed solution were added to a vial, which was kept at a 30℃ for 6 h.

Surface modification of Au NRs.

Au NRs were modified with biomolecules for bioassay. Formation of a self-assembled monolayer (SAM) on the surface of Au NRs was conducted using the modified protocol reported by the Petri-Fink group.[36] Au NRs were washed twice by centrifugation at 10,000 rpm for 10 min. Then, 50 μl of 1 mg/ml poly(ethylene glycol) 2-mercaptoethyl ether acetic acid was added to 2 ml of optically normalized Au NRs, which was then kept at a 50 ℃ for 12 h. The resulting solution was washed to remove residual poly(ethylene glycol) 2-mercaptoethyl ether acetic acid. The Au NRs with SAM were re-dispersed in MES buffer (pH 6.5) with TWEEN® 20 (0.25%). To immobilize antibodies, EDC/NHS coupling was conducted to activate carboxylate-terminal groups for 15 min. After washing twice by centrifugation at

10,000 rpm for 10 min, primary antibodies (M5, 150 kDa, A/California/06-2009) for HA1 (H1N1, 36.28 kDa, A/California/06-2009) were added to the system, and the Au NRs were shaken for 12 h. The conjugated Au NRs were then washed five times by centrifugation at 10,000 rpm for 10 min with 20 mM PBS (phosphate buffer saline, pH 7.6) solution and then re-dispersed in PBS to remove TWEEN® 20, which facilitated the immunochemical reaction between antigens and antibodies. Finally, the HA1 target analytes were introduced and incubated for 24 h.

Experimental setups

A magnetic stirrer (dimensions: 11 cm × 12 cm × 2 cm, field strength: 1 mT, Neuation, USA) was placed under the cuvette to generate an external rotating magnetic field. Throughout the entire biosensing experiment, the total volume of analytes (500 μL) was fixed. To clearly identify aggregation between antigen-bound Au NRs and MN-rings during the bioassay, we monitored both the well-defined LSPR spectral band of Au NRs and the periodic sigmoidal wave-like optical response of MN-rings under the external rotating magnetic field of the binary mixture. If there had been aggregation among nanoparticles in the binary mixture that severely affected the systems, a well-defined LSPR spectral band and periodically fluctuating wave-like optical response due to the presence of MN-rings could not be obtained.

Results and discussion

To achieve a binary mixture with Au NRs and MN-rings, homogeneous mixing of the two types of nanoparticles is of critical importance. Typical field effect-scanning electron microscopy (FE-SEM) images of each step are shown in Figure 1A-D. Highly uniform MN-

rings were synthesized by sequentially growing Pt rim-preferential on a 2D template Au nanodisks (Au NDs), etching of the Au core, and uniform coating of Ni on the Pt framework. Briefly, we utilized Au NDs as a removable template (d = 96±3 nm). Then, introduction of rim-preferential Pt onto the surface of Au NDs was affected by a thin silver layer on Au nanoplates, as previously developed in our group.[33] Concisely, this process comprised formation of a thin Ag layer on the Au template by adding a trace amount of $AgNO_3$, and the oxidized Ag^+ ions were reduced to Ag atoms on the Au {111} facets (i.e., the flat top and bottom terraces) by ascorbic acid. This thin layer of Ag plays an essential role in selective deposition of Pt at the edges. Pt atoms were exclusively reduced at the perimeter through the galvanic replacement reaction between Ag and Pt^{4+} ions due to the higher surface energy of the rim and vertex compared to the terrace of {112} facets (i.e., edges and vertices), leading to formation of Au@Pt nanodisks (Au@Pt NDs) with an augmented diameter of 117±3 nm. The inner Au part of the Au@Pt NDs was selectively etched to Au^+ by addition of Au^{3+} ions, resulting in the Pt framework (etching step). On the surface of Pt nanorings, reduction and deposition of Ni precursors were facilitated by the catalytic reaction of Pt initiating dissociation of the reducing agent, hydrazine, resulting in MN-rings (d = 134±5 nm) (Figure S2 shows a histogram of size distribution).[35] The reaction proceeds until the exposed Pt layer is completely covered by Ni but does not exceed a Ni thickness of 36 nm. The reduction power of hydrazine is not sufficient to induce nucleation of Ni without the assistance of Pt, which controls the thickness of the outer Ni layer up to 36 nm on the Pt nanorings. Thus, overgrowth of Ni on Pt nanorings over this thickness limit was automatically suppressed (Figure S3), leading to a homogeneous size distribution of the resulting MN-rings. A detailed structural and compositional analysis of the MN-rings was carried out by TEM and EDS line mapping images, as exhibited in Figure 1E-F. The dark central domains indicate heavier atoms (Pt), and the

light-colored peripheries show the deposited lighter atoms (Ni), confirmed by energy dispersive spectroscopy (EDS) mapping images (panels I-L). Interestingly, as Ni atoms were deposited onto the surface of the Pt nanorings, the entire surface developed a bumpy Ni granular surface due to lattice mismatch between Pt (lattice constant 0.3912 nm) and Ni (lattice constant 0.3499 nm).[37] The magnetic responsiveness of MN-rings was observable when a permanent magnet was attached to the side of the vial, as shown in the optical photographs (Figure 1G&H).

Of critical interest is comparison of the UV-visible NIR spectrum obtained following each compositional change (Figure S1). The optical spectrum of the as-prepared pure Au NDs (d = 96±3 nm) showed a distinct dipole resonance peak at 734 nm. As the surface of Au NDs was covered by Pt (thickness of Pt is approximately 14 nm), the mode redshifted to 875 nm, resulting from surface plasmon coupling between the core Au and Pt on the rims,[33,38] in addition to significant band-damping. After selective etching of the core Au part and Ni layer formation around the Pt nanorings, the dipole mode completely disappeared, and a broad featureless extinction appears over the entire spectral range, as depicted with blue and bluish-green traces in Figure S1. This effect is due to the optical inactivity of both Pt and Ni in the observed spectral window.

We investigated the extinction profiles of Au NDs, Au@Pt NDs, Pt nanorings, and MN-rings dispersed in water with and without a rotating magnetic field ($\omega/2\pi$ = 1.67 Hz, measured at 700 nm at a time interval of 25 ms) (Figure 2A). In the absence of an external rotating magnetic field, only thermal fluctuation (due to Brownian motion) was observed in the variation of extinction intensity with time (upper four traces in black, red, blue, and green). In contrast, upon application of a rotational magnetic field, only MN-rings showed a sigmoidal

pattern in extinction intensity (bottom green trace in Figure 2A). Additionally, FFT conversion exhibited a sharp peak at 3.33 Hz (bottom green line in Figure 2B). Although there are several other frequency peaks in a higher-frequency domain representing various behaviors of MN-rings under the given rotating magnetic field (for example, rotation, self-rotation, translational motion, asynchronous motion), we only considered the dominant frequency peaks where intensity was highest as we applied a rotating magnetic field with various frequencies ($\omega/2\pi$ = 0.25, 1.67, 3.33, 5.00, 6.67, and 8.33 Hz), as in Figure 2C, and sequential FFT frequency shifts were observed, indicating an instantaneous response of the magnetically active MN-rings, shown in Figure 2D. The Ni coating layer needs to be sufficiently thick for successful magnetic modulation (Figure S3). It is noteworthy that the ring structure is advantageous in terms of local stirring (homogeneous mixing) and the measurement stability (constant extinction profile) during the magnetic modulation. As a control experiment, we synthesized the comparable size of spherical solid magnetic nanoparticles (Figure S4) and tested their stability under the magnetic rotation field (8.33 Hz) for 1000 sec, as shown in Figure 2E. The extinction profile exhibited the unstable fluctuation (larger standard deviation at the given point) and the consistent decrease in the extinction as a function of time, indicating the local aggregation among spherical nanoparticles. Additionally, the solid magnetic nanoparticles (MNSs) are more susceptible to the gravitational force and the floating time is shorter than MN-rings. We believe that the inner empty space attribute to the longer floating time of MN-rings while they rotate under magnetic modulation. Therefore, it is critical to control the shape of magnetic nanoparticle to prevent the undesirable aggregation or precipitation, leading to the reliable and reproducible detection with the current binary nanoparticle detection method. Additionally, there was no noticeable aggregation under the given magnetic rotation, which was confirmed by the reversible variation in the frequency peak positions as rotating speed was consecutively

increased and decreased for several cycles over a total of 40 min of measurement Figure 2F. The ring-shape is superior to the analogous spherical shape in those aspects.

As a proof of concept, we mixed as-prepared MN-rings (15 fM) with various sizes of Au NRs (40 fM) and then tested their signal-to-noise ratio dependency on the peak shift ($\Delta\lambda$) from the observation frequency. In the first set of experiment Au nanorod were prepared through the seed-mediated synthesis method,[13] as the diameter of the Au NRs increased, the peak wavelength was systematically redshifted and gradually deviated from the observation wavelength, as in Figure 3A (Figure S6). Under magnetic rotation, the extinction fluctuation at 740 nm was monitored as a function of time, and a typical sigmoidal function was generated, as shown in Figure 3B. As the peak shift ($\Delta\lambda$) from the observation wavelength (740 nm) increases, the sigmoidal function becomes more distinct, leading to increased frequency peak intensity after FFT conversion (Figure 3C). The smaller is the LSPR band overlap with fluctuating extinction of MN-rings, the larger is the amplitude of the sigmoidal function, leading to increased frequency peak intensity (peak intensity with lower aspect ratio minus peak intensity with highest aspect ratio), as shown in Figure 3D.

In contrast, using a large amount of MN-rings (more than ca. 15 fM) would cause the rotational free volume of the rings to interfere with neighboring MN-rings. Eventually, MN-rings collide with each other, decreasing the amplitude of sigmoidal functions because of asynchronous rotation. The optimal concentration of MN-rings given the maximum amplitude in the sigmoidal function was determined to be 15 fM (Figure S5). Under this condition, the ratio between MN-rings and Au NRs can be optimized for operation of this sensing platform; the optimized ratio between MN-rings and Au NRs was 2.7. If the ratio deviates from this value,

the excitation of Au NRs is too low or too high; in both cases, there is little effect on the sigmoidal fluctuation of MN-ring extinction, which generates inconsistent sensing (Figure S7**)**.

Of critical importance is detection of bio-recognition on Au NRs when the mixture is modulated with magnetic rotation in the presence of MN-rings. Au NRs with a diameter d = 48±7 nm showed two characteristic LSPR dipole modes. The dipole mode at 740 nm was generated by collective oscillation of surface free electrons along the long axis. It is well known that the longitudinal mode of Au NRs is more sensitive to refractive index change of the surroundings than the transverse dipole mode at shorter wavelengths.[39] The Au NRs conjugated with an antibody of influenza A virus (1 nM of M5, IgG type) exhibited a peak shift from 740 to the longer wavelength (however, it is not easy to pick the peak position clearly from the band, but the band damping is clearly noticeable) after adding 1 pM of HA1 (influenza virus) (Figure S8).[40] The band became broader and dampened as bio-recognition reactions occurred on the Au NRs, as shown in Figure 4A, producing lack of clarity in antigen detection by direct monitoring of the peak shifts.

In the second set of experiments, we mixed Au NRs with MN-rings and applied a rotational magnetic field of 1.67 Hz. As the concentration of antigens was increased and the peak wavelength consequently redshifted, the sigmoidal functions became more distinct (from top to bottom in Figure 4B) due to the decrease of accumulated noise from the Au NRs LSPR band. After FFT conversion, the corresponding peak frequencies exhibited different peak intensities (red, blue, green, bluish-green traces in panel C) compared to the Au NRs modified only with antibody (top black line), as shown in Figure 4C. Additionally, the primary frequency peak positions (3.33 Hz) for all the samples were identical; therefore, background subtraction (peak intensity with antigen/antibody minus peak intensity with antibody) enabled facile

detection of antigens, as in Figure 4D. As a control experiment, we measured the peak shift of LSPR as a function of target analyte concentration, varying from 1 fM to 1 pM. The conventional LSPR sensing method is based on the direct observation of peak shift that is induced by the change in the dielectric constant of surrounding medium. With this method, the peak shift was not detectable when the concentration is less than 10 fM (black trace, Figure 4E). On the other hand, when the concentration is larger than 100 fM, the detection sensitivity (the slope between concentration and magnitude of peak shift) becomes too small to differentiate the concentration (in other words, the dynamic range is narrow). Additionally, the degree of peak damping increases as the concentration increases (bluish-green trace, Figure 4E). With the conventional LSPR sensing, binding event of the target molecules to the recognition sites is solely monitored by the LSPR band shift, and the band damping often obscures the recognition of peak-shift. In contrast, we observed consistent increase of frequency peak intensities as we increased the concentration of the target analytes from 1 fM to 1 pM (Figure 4F). This is resulted from the combined effect of the shifts of LSPR band to longer wavelength and the band damping. It is noteworthy that both lead to the less overlapping with fluctuating extinction of MN-rings, eventually leading to the larger amplitude of a sigmoidal function. Interestingly, our biosensing platform can detect the concentration of HA1 as low as 1 fM, which is one order of magnitude lower than the detection limit achieved by the conventional LSPR method (10 fM). With the binary mixture sensing, not only the peak shift but also band damping contributes to the decreased noise in the sigmoidal fluctuation of extinction, leading to higher sensitivity, lower detection limits, and more tailorable dynamic range, than conventional LSPR sensing. (Figure 4E (conventional LSPR sensing) and F (binary mixture sensing))

Conclusion

In contrast to conventional biosensors (a stagnant assay without perturbation) that use the peak shift of a localized surface plasmon resonance of Au NRs, the mixture of Au NRs and MN-rings were modulated with an external rotating magnetic field (a dynamic assay with magnetic perturbation), while observing the extinction fluctuations. As antigens bind to recognition sites on the Au NRs, their periodic profile of extinction changed, resulting from peak shifts and damping of LSPR bands, which led to decrease of noise in the fluctuating extinction profile. The obtained periodic extinction with time was converted to a frequency domain function where the signal-to-noise ratios of the peaks were evaluated to monitor surface bio-recognition on Au NRs. Using this biosensor platform, the limit of detection for HA1 was enhanced by tow orders of magnitude compared to those of conventional LSPR methods, indicated our system is highly effective. Given that there are various shapes of nanostructures available, a myriad of combinations among them will open a new avenue for biosensing.

Acknowledgements

This research was supported by the Basic Science Research Program through the National Research Foundation of Korea (NRF) funded by the Ministry of Science, ICT & Future Planning (NRF-2017R1A2B3002796), the National Research Foundation of Korea (NRF) grant funded by the Korea government (MSIP) (NRF-2017R1A5A1015365).

Supporting Information

UV-Vis spectra of shape evaluation, histogram representing size distribution, TEM

images of various thicknesses of MN-rings, synthesis of MNSs, SFT of different concentrations of MN-rings, FE-SEM images of various sizes of Au NRs, optimization of conc. of Au NRs with 15 fM of MN-rings in a binary mixture (sensing platform), DLS and UV-vis-NIR spectrophotometer confirming surface modification of Au NRs. "This material is available free of charge via the Internet at http://pubs.acs.org."

Conflict of interest

The authors declare no conflict of interest.

References

(1) Hutter, E.; Fendler, J. H., Exploitation of Localized Surface Plasmon Resonance, *Adv Mater,* **2004**, 16, 1685-1706.

(2) Jones, M. R.; Osberg, K. D.; Macfarlane, R. J.; Langille, M. R.; Mirkin, C. A., Templated techniques for the synthesis and assembly of plasmonic nanostructures, *Chem Rev*, **2011**, 111, 3736-3827.

(3) Kelly, K. L.; Coronado, E.; Zhao, L. L.; Schatz, G. C., The Optical Properties of Metal Nanoparticles: The Influence of Size, Shape, and Dielectric Environment, *J Phys Chem B*, **2003**, 107, 668-677.

(4) He, S. S.; Hai, J.; Li, T. R.; Liu, S.; Chen, F. J.; Wang, B. D., Photochemical strategies for the green synthesis of ultrathin Au nanosheets using photoinduced free radical generation and their catalytic properties, *Nanoscale*, **2018**, 10, 18805-18811.

(5) Crawford, S. E.; Hartmann, M. J.; Millstone, J. E., Surface Chemistry-Mediated Near-Infrared Emission of Small Coinage Metal Nanoparticles, *Accounts Chem Res*, **2019**, 52, 695-703.

(6) Yu, C. X.; Irudayaraj, J., Multiplex Biosensor Using Gold Nanorods, *Anal Chem*, **2007**, 79, 572-579.

(7) Mayer, K. M.; Hafner, J. H., Localized Surface Plasmon Resonance Sensors, *Chem Rev,* **2011**, 111, 3828-3857.

(8) Chen, Y.; Munechika, K.; Ginger, D. S., Bioenabled Nanophotonics, *Mrs Bull*, **2008**, 33, 536-542.

(9) Choi, Y.; Choi, J. H.; Liu, L.; Oh, B. K.; Park, S., Optical Sensitivity Comparison of Multiblock Gold–Silver Nanorods Toward Biomolecule Detection: Quadrupole Surface Plasmonic Detection of Dopamine, *Chem Mater*, **2013**, 25, 919-926.

(10) Shen, Y.; Zhou, J. H.; Liu, T. R.; Tao, Y. T.; Jiang, R. B.; Liu, M. X.; Xiao, G. H.; Zhu, J. H.; Zhou, Z. K.; Wang, X. H.; Jin, C. J.; Wang, J. F., Plasmonic gold mushroom arrays with refractive index sensing figures of merit approaching the theoretical limit, *Nat Commun*, **2013**, 4.

(11) Jeong, H. H.; Mark, A. G.; Alarcon-Correa, M.; Kim, I.; Oswald, P.; Lee, T. C.; Fischer, P., Dispersion and shape engineered plasmonic nanosensors, *Nat Commun*, **2016**, 7.

(12) Wiley, B. J.; Chen, Y. C.; McLellan, J. M.; Xiong, Y. J.; Li, Z. Y.; Ginger, D.; Xia, Y. N., Synthesis and Optical Properties of Silver Nanobars and Nanorice, *Nano Lett*, **2007**, 7, 1032-1036.

(13) Vigderman, L.; Khanal, B. P.; Zubarev, E. R., Functional gold nanorods: synthesis, self-assembly, and sensing applications, *Adv Mater*, **2012**, 24, 4811-4841.

(14) Dondapati, S. K.; Sau, T. K.; Hrelescu, C.; Klar, T. A.; Stefani, F. D.; Feldmann, J., Label-free Biosensing Based on Single Gold Nanostars as Plasmonic Transducers, *Acs Nano*, **2010**, 4, 6318-6322.

(15) Chen, H. J.; Kou, X. S.; Yang, Z.; Ni, W. H.; Wang, J. F., Shape- and Size-Dependent Refractive Index Sensitivity of Gold Nanoparticles, *Langmuir*, **2008**, 24, 5233-5237.

(16) Zhao, J.; Das, A.; Zhang, X. Y.; Schatz, G. C.; Sligar, S. G.; Van Duyne, R. P., Resonance Surface Plasmon Spectroscopy: Low Molecular Weight Substrate Binding to Cytochrome P450, *J Am Chem Soc*, **2006**, 128, 11004-11005.

(17) Wy, Y.; Lee, S.; Wi, D. H.; Han, S. W., Colloidal Clusters of Bimetallic Core–Shell Nanoparticles for Enhanced Sensing of Hydrogen in Aqueous Solution, *Part Part Syst Char*, **2018**, 35.

(18) Hall, W. P.; Ngatia, S. N.; Van Duyne, R. P., LSPR Biosensor Signal Enhancement Using Nanoparticle-Antibody Conjugates, *J Phys Chem C*, **2011**, 115, 1410-1414.

(19) Xu, Z. C.; Hou, Y. L.; Sun, S. H., Magnetic Core/Shell Fe3O4/Au and Fe3O4/Au/Ag Nanoparticles with Tunable Plasmonic Properties, *J Am Chem Soc*, **2007**, 129, 8698-+.

(20) Zhang, Y.; DaSilva, M.; Ashall, B.; Doyle, G.; Zerulla, D.; Sands, T. D.; Lee, G. U., Magnetic manipulation and optical imaging of an active plasmonic single-particle Fe-Au nanorod, *Langmuir*, **2011**, 27, 15292-15298.

(21) Wang, M. S.; Yin, Y. D., Magnetically Responsive Nanostructures with Tunable Optical Propertie, *J Am Chem Soc*, **2016**, 138, 6315-6323.

(22) Jung, I.; Jang, H. J.; Han, S.; Acapulco, J. A. I.; Park, S., Magnetic Modulation of Surface Plasmon Resonance by Tailoring Magnetically Responsive Metallic Block in Multisegment Nanorods, *Chem Mater*, **2015**, 27, 8433-8441.

(23) Wei, Q. S.; Song, H. M.; Leonov, A. P.; Hale, J. A.; Oh, D. M.; Ong, Q. K.; Ritchie, K.; Wei, A., Gyromagnetic Imaging: Dynamic Optical Contrast Using Gold Nanostars with Magnetic Cores, *J Am Chem Soc*, **2009**, 131, 9728-9734.

(24) Li, Z. W.; Yang, F.; Yin, Y. D., Smart Materials by Nanoscale Magnetic Assembly, *Adv Funct Mater*, **2020**, 30.

(25) Jung, I.; Yoo, H.; Jang, H. J.; Cho, S.; Lee, K.; Hong, S.; Park, S., Fourier Transform Surface Plasmon Resonance (FTSPR) with Gyromagnetic Plasmonic Nanorods, *Angew Chem Int Edit,* **2018**, 57, 1841-1845.

(26) Jung, I.; Ih, S.; Yoo, H.; Hong, S.; Park, S., Fourier Transform Surface Plasmon Resonance of Nanodisks Embedded in Magnetic Nanorods, *Nano Lett*, **2018**, 18, 1984-1992.

(27) Kwak, M.; Jung, I.; Kang, Y. G.; Lee, D. K.; Park, S., Multi-block magnetic nanorods for controlled drug release modulated by Fourier transform surface plasmon resonance, *Nanoscale*, **2018**, 10, 18690-18695.

(28) Levin, C. S.; Hofmann, C.; Ali, T. A.; Kelly, A. T.; Morosan, E.; Nordlander, P.; Whitmire, K. H.; Halas, N. J., Magnetic-plasmonic core-shell nanoparticles, *Acs Nano*, **2009**, 3, 1379-1388.

(29) Fan, Z.; Shelton, M.; Singh, A. K.; Senapati, D.; Khan, S. A.; Ray, P. C., Multifunctional Plasmonic Shell-Magnetic Core Nanoparticles for Targeted Diagnostics, Isolation, and Photothermal Destruction of Tumor Cells, *Acs Nano*, **2012**, 6, 1065-1073.

(30) Guo, J.; Kim, K.; Leia, K. W.; Fan, D. L., Ultra-durable rotary micromotors assembled from nanoentities by electric fields, *Nanoscale*, **2015**, 7, 11363-11370.

(31) Khanal, B. P.; Zubarev, E. R., Purification of High Aspect Ratio Gold Nanorods: Complete Removal of Platelets, *J Am Chem Soc*, **2008**, 130, 12634-+.

(32) Millstone, J. E.; Park, S.; Shuford, K. L.; Qin, L. D.; Schatz, G. C.; Mirkin, C. A., Observation of a Quadrupole Plasmon Mode for a Colloidal Solution of Gold Nanoprisms, *J Am Chem Soc*, **2005**, 127, 5312-5313.

(33) Jang, H. J.; Hong, S.; Ham, S.; Shuford, K. L.; Park, S., Site-specific growth of a Pt shell on Au nanoplates: tailoring their surface plasmonic behavior, *Nanoscale,* **2014**, 6, 7339-7345.

(34) Park, S.; Yang, P. X.; Corredor, P.; Weaver, M. J., Transition Metal-Coated Nanoparticle Films: Vibrational Characterization with Surface-Enhanced Raman Scattering, *J Am Chem Soc*, **2002**, 124, 2428-2429.

(35) Grzelczak, M.; Rodriguez-Gonzalez, B.; Perez-Juste, J.; Liz-Marzan, L. M., Quasi-Epitaxial Growth of Ni Nanoshells on Au Nanorods, *Adv Mater*, **2007**, 19, 2262-+.

(36) Kinnear, C.; Dietsch, H.; Clift, M. J. D.; Endes, C.; Rothen-Rutishauser, B.; Petri-Fink, A., Gold Nanorods: Controlling Their Surface Chemistry and Complete Detoxification by a Two-Step Place Exchange, *Angew Chem Int Edit*, **2013**, 52, 1934-1938.

(37) Schmid, M.; Biedermann, A.; Stadler, H.; Slama, C.; Varga, P., Precision Measurements of the Lattice Constants of Twelve Common Metals, *Appl Phys a-Mater*, **1992**, 55, 468-475.

(38) Straney, P. J.; Marbella, L. E.; Andolina, C. M.; Nuhfer, N. T.; Millstone, J. E., Decoupling Mechanisms of Platinum Deposition on Colloidal Gold Nanoparticle Substrates, *J Am Chem Soc*, **2014**, 136, 7873-7876.

(39) Lee, K. S.; El-Sayed, M. A., Gold and Silver Nanoparticles in Sensing and Imaging: Sensitivity of Plasmon Response to Size, Shape, and Metal Composition, *J Phys Chem B*, **2006**, 110, 19220-19225.

(40) Link, S.; El-Sayed, M. A.; Mohamed, M. B., Simulation of the Optical Absorption Spectra of Gold Nanorods as a Function of Their Aspect Ratio and the Effect of the Medium Dielectric Constant, *J Phys Chem B*, **2005**, 109, 10531-10532.

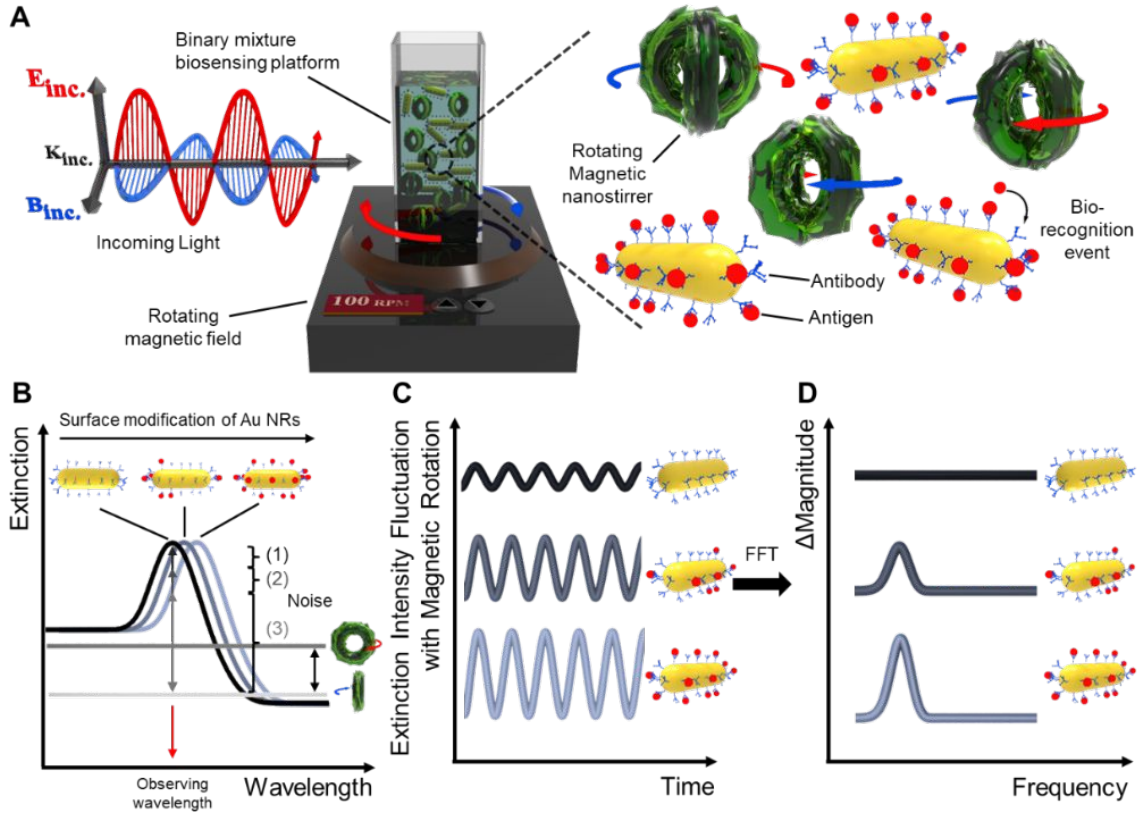

Scheme 1. Schematic illustration of the experimental setup. (A) While applying an external rotating magnetic field to the samples in a cuvette, the optical response of samples was monitored through UV-vis spectroscopy. Magnetically responsive Pt@Ni nanorings (magnetic nanostirrers, MN-rings) periodically fluctuate under the external rotating magnetic field. (B) When the optical response of the binary mixture of biomolecule-modified Au NRs and MN-rings was observed, due to the LSPR characteristics of Au NRs, extinction intensity fluctuation with magnetic rotation attributed to the back and forth movement of MN-rings was perturbed. This perturbation decreased as the LSPR band of Au NRs was shifted by modifying the surface of Au NRs at the fixed observation wavelength. (C, D) Optical response of the binary mixture of Au NRs and MN-rings under the external rotating magnetic field is demonstrated as a periodic fluctuating wave-like function under the time domain. After FFT conversion, the dominant peak is represented on the frequency domain. As the concentration of target analytes increased, the magnitude intensity increased.

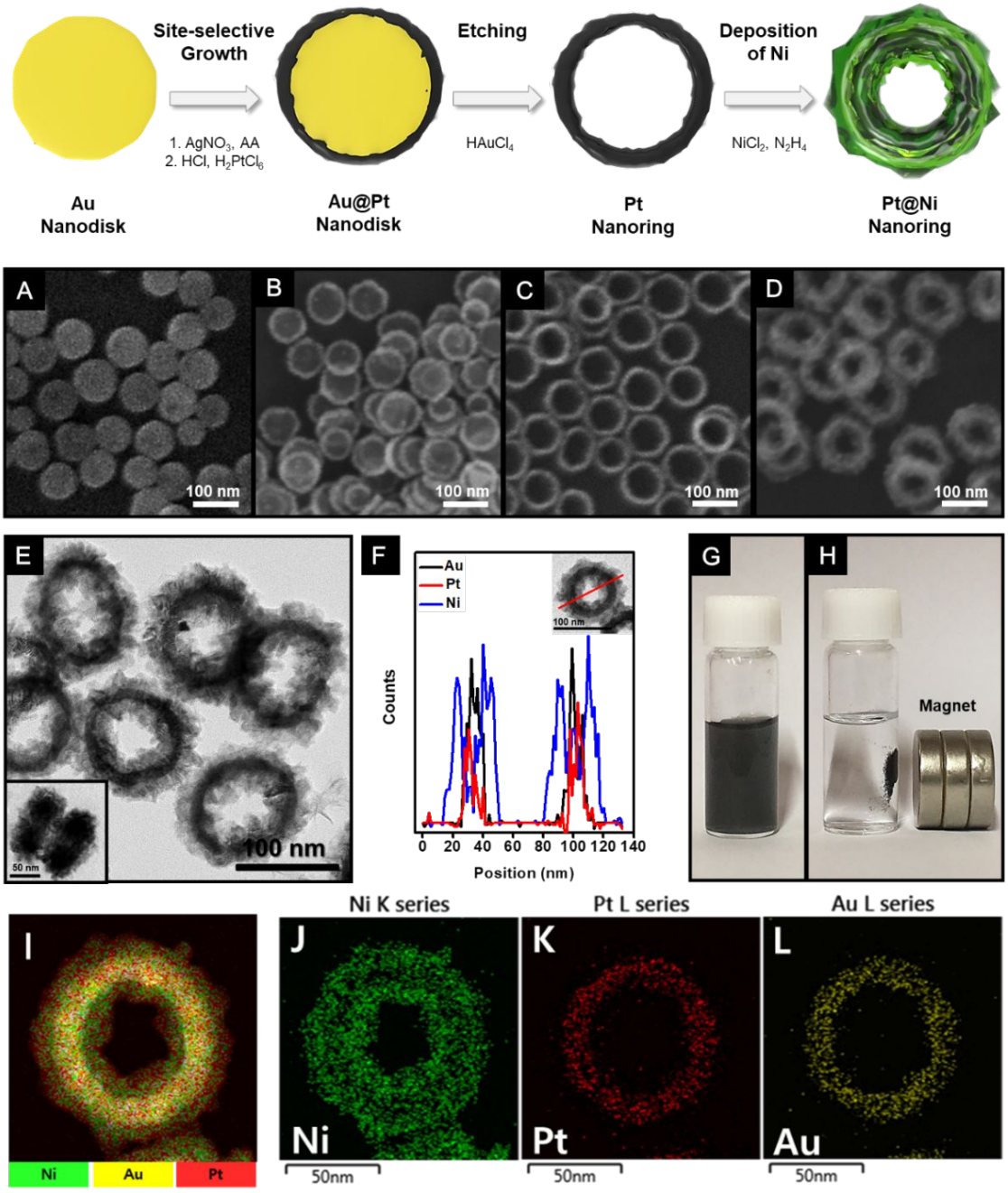

Figure 1. Schematic of experimental procedures for synthesizing Ni Magnetic Nanorings (MN-rings). (A-D) FE-SEM images of Au NDs, Au@Pt NDs, Pt N-rings, and MN-rings. (E) An HR-TEM image and (F) EDS line mapping of MN-rings. Line mapping was conducted along the red line in the inset image (black line: Au; red line: Pt; blue line: Ni). (G) Optical photographs of MN-rings dispersed in water after sonication and (H) adsorbed to the walls of a vial due to a permanent magnet. (I) Combined EDS elemental mapping showing distribution of Ni (green), Au (yellow), and Pt (red). (J-L) Individual EDS elemental mapping of (J) Ni, (K) Pt, and (L) Au in MN-ring.

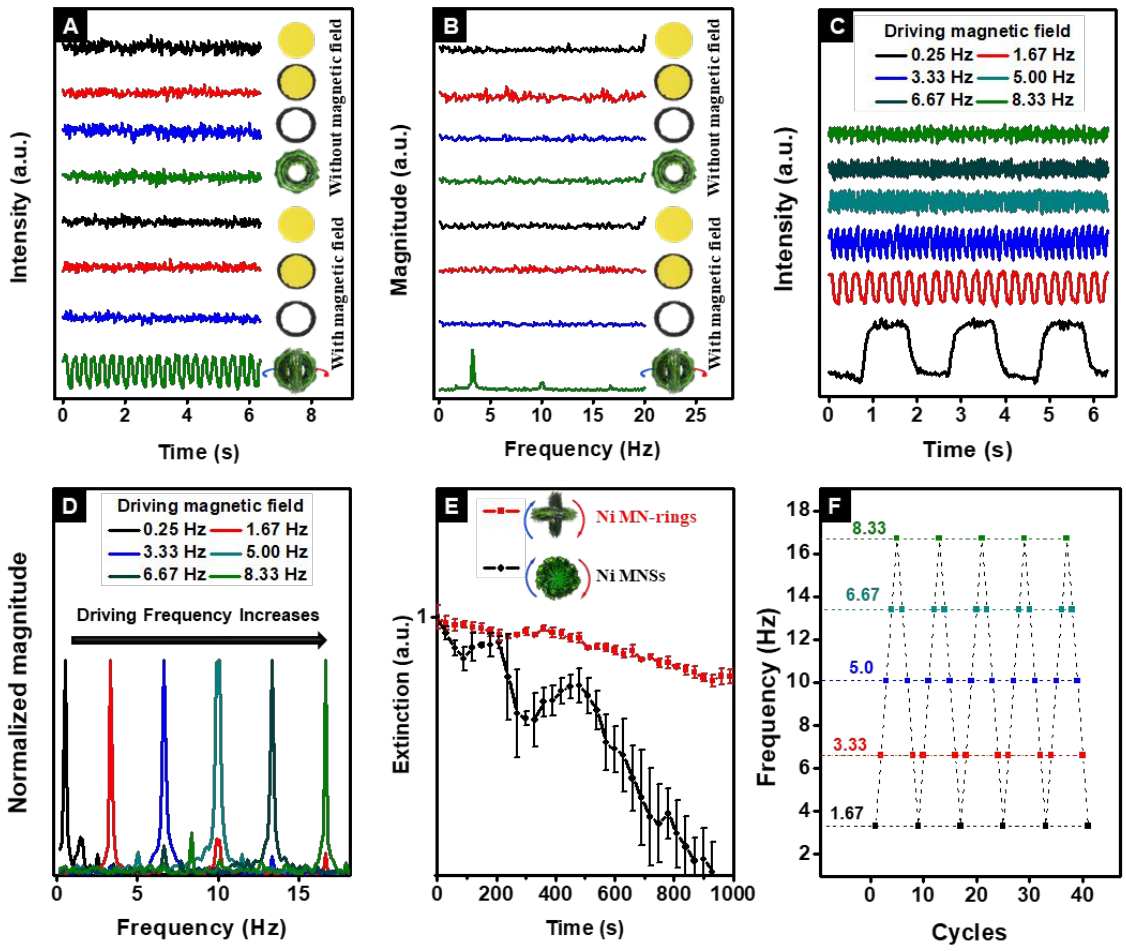

Figure 2. Magnetic modulation of Au NDs, Au@Pt NDs, Pt nanorings, and MN-rings. (A) Optical responses of Au NDs (black line), Au@Pt NDs (red line), Pt nanorings (blue line), and MN-rings (green line) with/without an external rotating magnetic field of frequency $\omega/2\pi$ = 1.67 Hz as a function of time. (B) Corresponding FFT plot of the optical response of Au NDs (black line), Au@Pt NDs (red line), Pt nanorings (blue line), and MN-rings (green line) with/without applying a rotating magnetic field (1.67 Hz). (C) MN-rings optical response to the rotating magnetic field (from $\omega/2\pi$ = 0.25 to 8.33 Hz) as a function of time (time interval of 25 ms) at the measuring wavelength of 700 nm. (D) Consecutive FFT frequency shifts as the frequency of applied frequency was increased from 0.25 to 8.33 Hz. (E) Stability test of MN-rings vs MNSs under applying magnetic field (8.33 Hz) for 1000 sec (Measuring wavelength : 700 nm). (F) Stability test of MN-rings. We consecutively sped up and slowed down the driving magnetic fields and measured the peak positions after Fourier transform.

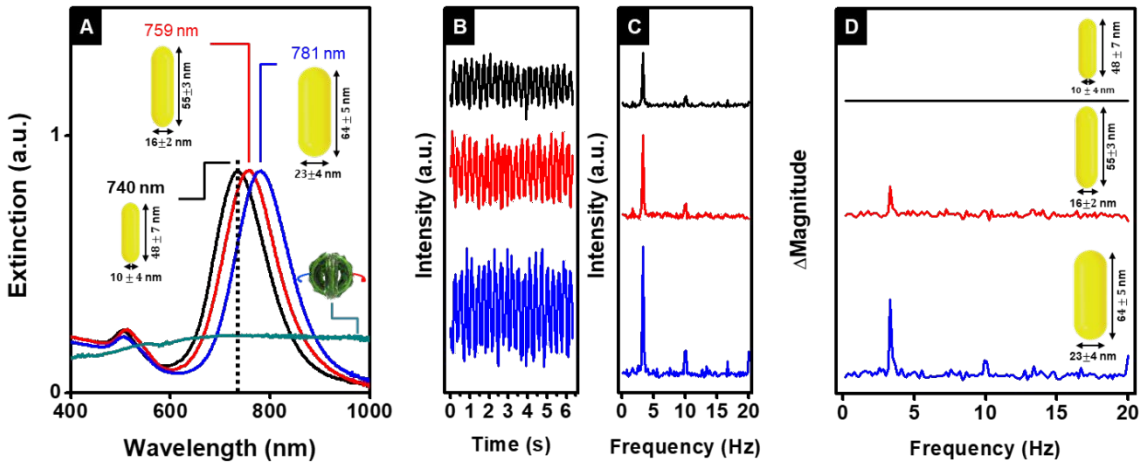

Figure 3. Optical characterization and binary mixtures of Au NRs and MN-rings. (A) As the size of Au NRs increased, the peak position of the LSPR band of Au NRs was easily tuned. (B) At the fixed observation wavelength, a signal generated by periodically fluctuating MN-rings was perturbed due to the presence of Au NRs. (C) As the size of Au NRs increased, the peak position of the LSPR spectral band deviated from the fixed observation wavelength, which leads to the sigmoidal function becomes more distinct, leading to increased frequency peak intensity after FFT conversion of a wave-like periodic signal obtained from the binary mixture of Au NRs and MN-rings. (D) Peak intensity with the highest aspect ratio minus peak intensity with a lower aspect ratio.

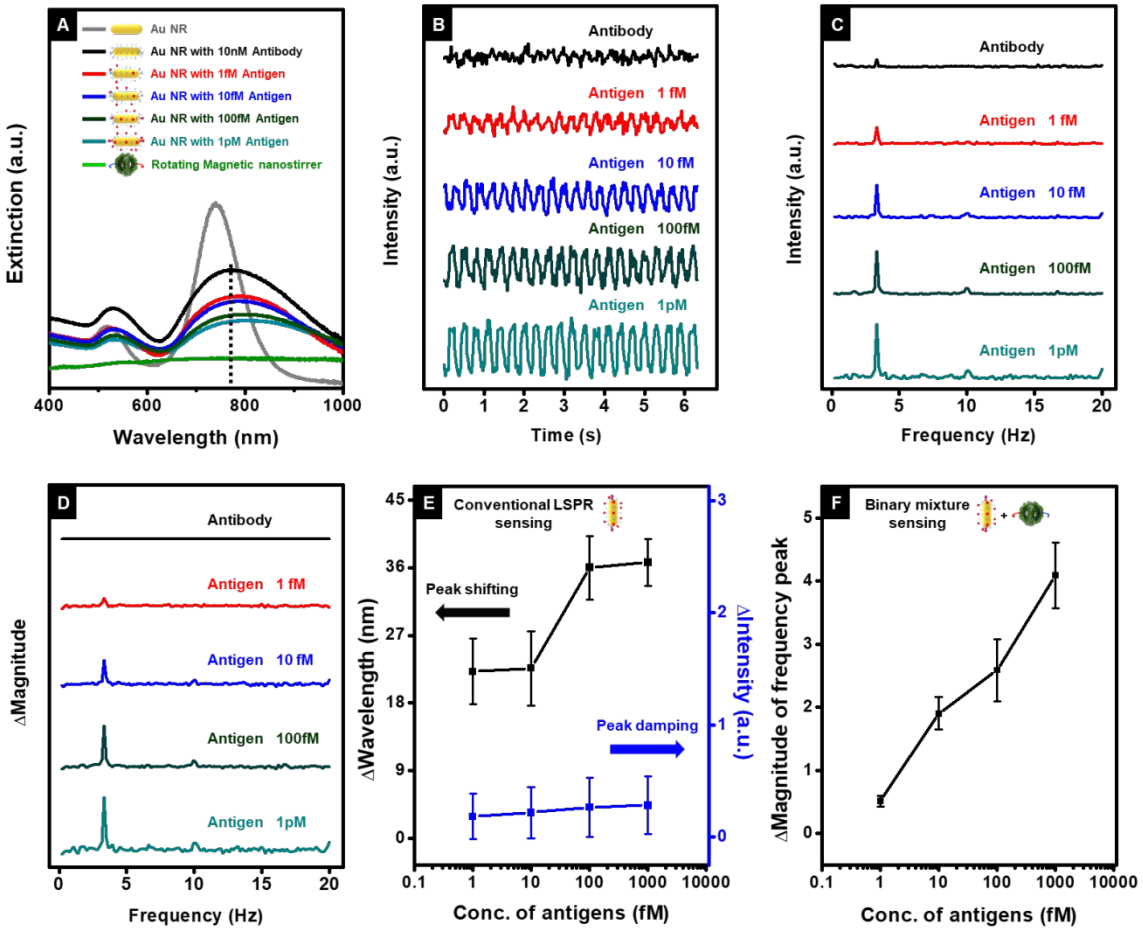

Figure 4. Surface modification of Au NRs with biomolecules and bioassay based on the binary mixture biosensing platform. (A) Surface modification of Au NRs with antibodies and antigens was monitored by observing the LSPR spectral band shift of the dipole mode of Au NRs. (B) Optical response of the binary mixture (MN-rings and different concentrations of target-bound Au NRs) under a magnetic rotating field. (C) Frequency domain peak after FFT conversion of the optical response represented by (B). (D) Peak intensity with antigen/antibody minus peak intensity with antibody. (E) Conventional LSPR sensing, indicating the peak shift (black trace) and band damping (blue trace) as a function of concentration. (F) Calibration curve based on binary mixture sensing.

Table of Contents (TOC) / Abstract (ABS) Graphic